Photovoltage field–effect transistors

Valerio Adinolfi[1] & Edward H. Sargent[1]

The detection of infrared radiation enables night vision, health monitoring, optical communications and three-dimensional object recognition. Silicon is widely used in modern electronics, but its electronic bandgap prevents the detection of light at wavelengths longer than about 1,100 nanometres. It is therefore of interest to extend the performance of silicon photodetectors into the infrared spectrum, beyond the bandgap of silicon[1,2]. Here we demonstrate a photovoltage field-effect transistor that uses silicon for charge transport, but is also sensitive to infrared light owing to the use of a quantum dot light absorber. The photovoltage generated at the interface between the silicon and the quantum dot, combined with the high transconductance provided by the silicon device, leads to high gain (more than 10^4 electrons per photon at 1,500 nanometres), fast time response (less than 10 microseconds) and a widely tunable spectral response. Our photovoltage field-effect transistor has a responsivity that is five orders of magnitude higher at a wavelength of 1,500 nanometres than that of previous infrared-sensitized silicon detectors[3]. The sensitization is achieved using a room-temperature solution process and does not rely on traditional high-temperature epitaxial growth of semiconductors (such as is used for germanium and III–V semiconductors)[4,5]. Our results show that colloidal quantum dots can be used as an efficient platform for silicon-based infrared detection, competitive with state-of-the-art epitaxial semiconductors.

The sensing of infrared radiation enables optical communications, night vision, health monitoring, spectroscopy and object inspection[6]. For this reason, many efforts have sought to integrate infrared detection onto silicon to combine infrared sensing with state-of-the-art electronics[7]. The ideal infrared photodetector must combine a fast response, high responsivity and low power consumption with facile fabrication[8]. Early efforts in this direction based on epitaxial semiconductors such as III-V and germanium[4,5,9] added complexity in the fabrication process due to epitaxial crystal growth requirements and the need to mitigate silicon contamination and doping[8].

Recently, black silicon was reported—an infrared-sensitive material obtained using laser treatment of the silicon surface[10–12]. However, this technology suffers from low responsivity ($10^{-2}-10^{-1}$ A W^{-1}) at infrared wavelengths[10].

Colloidal quantum dots (CQDs) have enabled photodetectors[13] that benefit from infrared sensitivity, high light absorption[14], wavelength tunability[15], low cost and room-temperature solution processing. However, CQDs have yet to be integrated successfully with silicon. In a heterojunction photodiode[16] or traditional photo-field-effect transistor (photo-FET), modest transport in the quantum dot solid limits the performance of the device. A new architecture is required that is not curtailed by the photoconductive effect—a mechanism that produces photodetectors that are either responsive but slow, or fast but unresponsive[17].

Here we present a Si:CQD photovoltage field-effect transistor (PVFET). It exploits a photovoltage that arises at the Si:CQD interface to control junction electrostatics. As a result, it modulates the conductivity of the silicon channel in proportion to incident light at wavelengths below that of the bandgap of silicon. The Si:CQD PVFET shows high responsivity in the infrared (1,300 nm and 1,500 nm) in excess of 10^4 A W^{-1}, a response that is faster than 10 μs, and dark current densities of $10^{-1}-10^1$ A cm^{-2} for a gate–source voltage of $V_{GS} = 0–3$ V. We explain and demonstrate the physical principles that govern the operation of the PVFET using simulations and analytical models, and show the potential of the device when fabricated using the state-of-the-art silicon techniques currently employed in the electronics industry.

In Fig. 1a we show the structure of the Si:CQD PVFET. A lightly p$^-$-type silicon channel is epitaxially grown on an n$^+$ silicon substrate that acts as a gate. The channel is contacted with ohmic aluminium source and drain (see Supplementary Information section S1). A thin n-doped CQD film is deposited on top of the silicon channel, creating an infrared-photosensitive gate. The source and drain were covered with a thick layer of insulating silicon nitride to prevent electrical contact between the photogate and the aluminium.

The means of deposition of the CQD layer is crucial to the operation of the device. The rectifying Si:CQD junction relies on the passivation of surface traps and providing energetic alignment between the two semiconductors. In the absence of judiciously engineered heterointerface passivation, the two semiconductors fail to produce an efficient rectifying heterojunction[16].

Figure 1e shows the transverse energy band diagram of the PVFET: the thin (1.6 μm) silicon p-doped layer is sandwiched between two n-type rectifying junctions and is therefore depleted at equilibrium (in the dark). Simulations (Fig. 1c, d) illustrate the working principles of the device. Upon optical illumination using 1,300-nm incident radiation (Fig. 1c), photocarriers are generated exclusively within the CQD solid. This produces a photovoltage at the interface via the photovoltaic effect—the same effect that produces an open-circuit voltage in solar cells. In the PVFET, this effective bias shrinks the depletion region and thereby increases the extent of the (undepleted) channel in the silicon. Figure 1d shows the density of holes (majority carriers) in the silicon channel in the dark and under 1,300-nm illumination.

We analyse the operation of the PVFET to further explain the physical mechanisms that govern its behaviour and compare its performance with that of other photodetector architectures (Fig. 2).

The gain as a function of the dark current for the PVFET, photodiodes, photoconductors and photo-FETs have been analysed (Fig. 2a). Photoconductors and photo-FETs (that is, previously developed CQD-based phototransistors) are treated together because the gain mechanism that governs these devices is the same: trap-assisted photoconductivity[18,19]. Diodes do not produce gain[20]; photoconductors and photo-FETs have a linear relationship between photoconductive gain G_P and dark current I_D: $G_P = \tau_l/\tau_t$, where τ_l is the trap lifetime and τ_t is the transit time within the channel, which is related to I_D through the electrical mobility (see Supplementary Information). The gain can be increased by decreasing the transit time, that is, by using a high-mobility channel (for example, graphene[18]); however, doing so increases the dark current.

In the PVFET, gain is adjusted by tuning the doping of the channel; the effect of the gate allows high gain at low dark current. The gain produced by the PVFET is $h\nu/q \times V_{ph}g_m/P_{opt}$ (see Supplementary Information section S3) where h is the Planck constant, ν is the optical
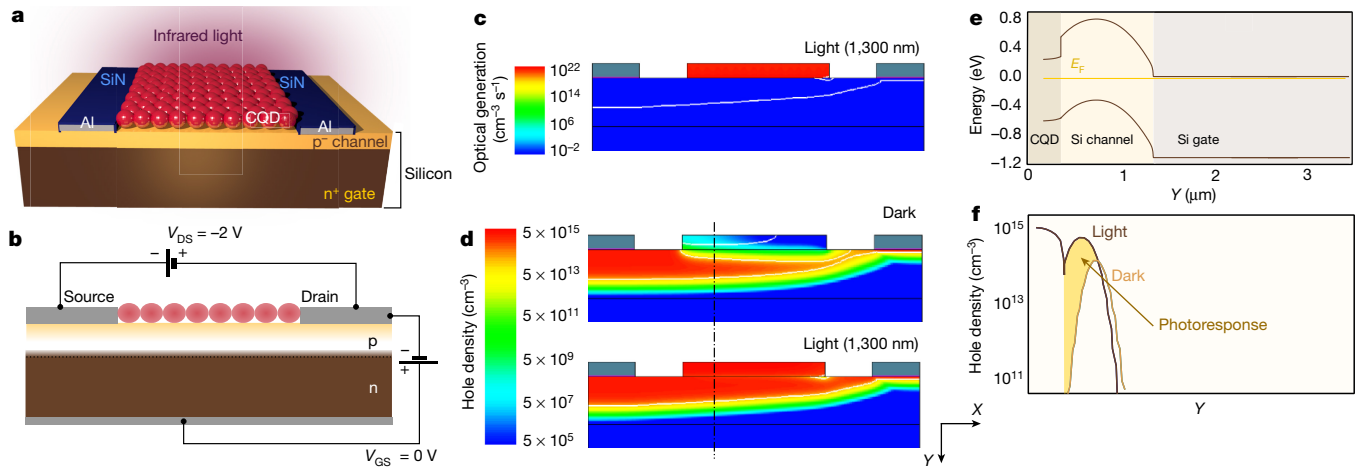
Figure 1 | Structure and physical principles of the PVFET. a, Three-dimensional model of the Si:CQD PVFET. **b**, Schematic of the electrical circuit showing the voltage bias. V_{DS}, source–drain voltage; V_{GS}, gate–source voltage. **c**, TCAD (Technology Computer Aided Design) simulation showing optical generation under excitation by 1,300-nm light. Photocarriers are generated exclusively in the CQD photogate (illustrated as red circles in **b**). The white line roughly corresponds to the boundary of the depletion region (as defined by the simulator). **d**, TCAD simulation showing the hole density (majority carriers) in the dark and under 1,300-nm illumination. The light signal produces a photovoltage, which causes the depletion region within the silicon channel to shrink; this results in an increase in the hole density and therefore in the channel conductivity. **e**, Band diagram at equilibrium (dark) in the transversal (vertical, Y) direction. E_F, Fermi energy. **f**, Hole density evaluated along the dash-dotted line in **d**: the hole density strongly increases under illumination compared to the dark equilibrium. As is standard practice, we use the photosensitive area to calculate the current density and other figures of merit such as the detectivity D^*. In a (photo-)FET, an additional scaling law is at work: the dark current scales as W/L (channel width/channel length)—an important design parameter that must also be taken into account.

frequency, q is the elemental charge, V_{ph} is the photovoltage, P_{opt} is the incident optical power and g_m is the transconductance of the PVFET, which is defined as $g_m = dI_{DS}/dV_{ph}$, where I_{DS} is the source–drain current. We compared this analytical model to fully self-consistent numerical simulations (TCAD) and found good agreement, especially at high current (Fig. 2a); the analytical model does not accurately capture the subthreshold regime.

Gain based on photovoltage and transconductance is distinct from photoconductive gain. It enables simultaneously high signal amplification and rapid response[20] (Fig. 2c). Whereas photoconductors and

photo-FETs are limited in speed by τ_l, and rely on traps to produce gain[13], the bandwidth of the PVFET is instead determined by the total capacitance, resulting in an operating frequency of $f = g_m/C_{TOT}$, where C_{TOT} is the total capacitance. As can be seen in Fig. 2c, whereas gain is generated in photoconductors and photo-FETs at the expense of speed (CQD photo-FETs are typically limited to response times in the range 0.001–1 s owing to the required high values of τ_l)[19,21], in the PVFET, high gain (high g_m) leads to a rapid response time. This gain mechanism allows for a large $G_P \times BW$ product, as shown in Fig. 2b. Here, we achieve experimentally a $G_P \times BW$ product of $10^4 \times 10^5\,\mathrm{s}^{-1}$
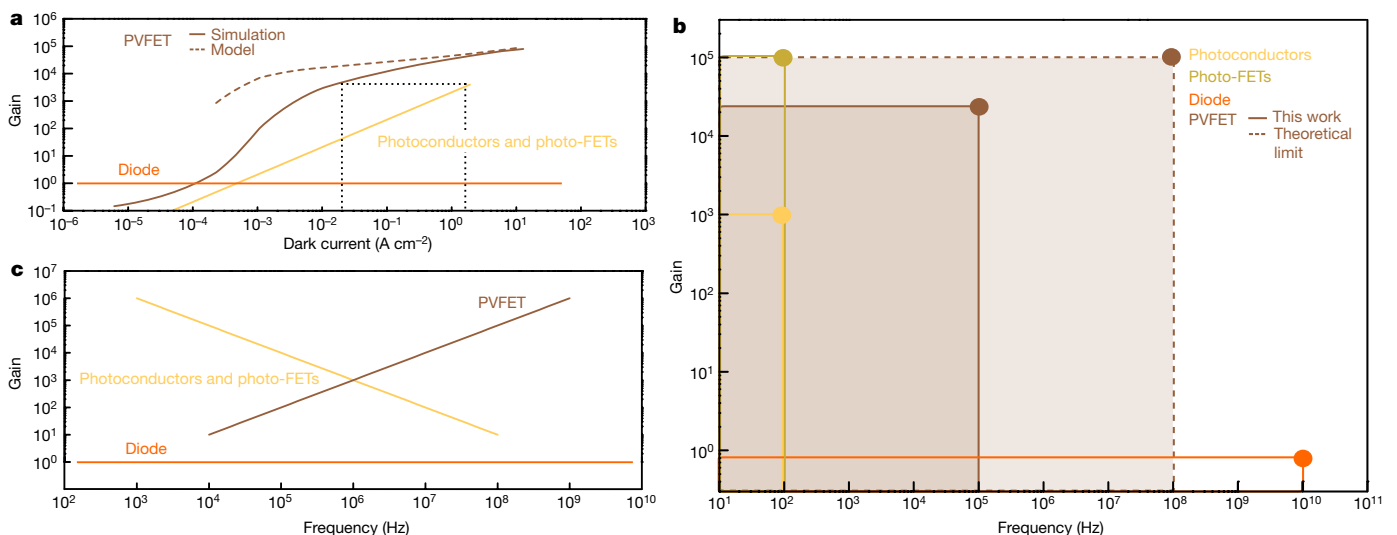

Figure 2 | Numerical and analytical analysis of the PVFET. a, Model of the gain as a function of the dark current for diodes, photoconductors and photo-FETs, and the PVFET architecture. Two lines are drawn for the PVFET: the solid line was computed using TCAD; the dashed line was evaluated using the analytical model. The dotted lines are a guide to the eye, highlighting the difference in dark current at the same gain. **b**, Gain–frequency plot for diodes, photo-FETs (CQD-based), photoconductors (CQD-based) and the PVFET. Experimental results and the theoretical limit are reported for the Si:CQD PVFET. The $G_P \times BW$ product is illustrated by the area of the coloured shading. **c**, Model showing the relationship between gain and frequency for the PVFET, and photoconductors and photo-FETs. Whereas the response time in photoconductors and photo-FETs is increased at the expenses of gain, for the PVFET gain increases for increasing frequencies.
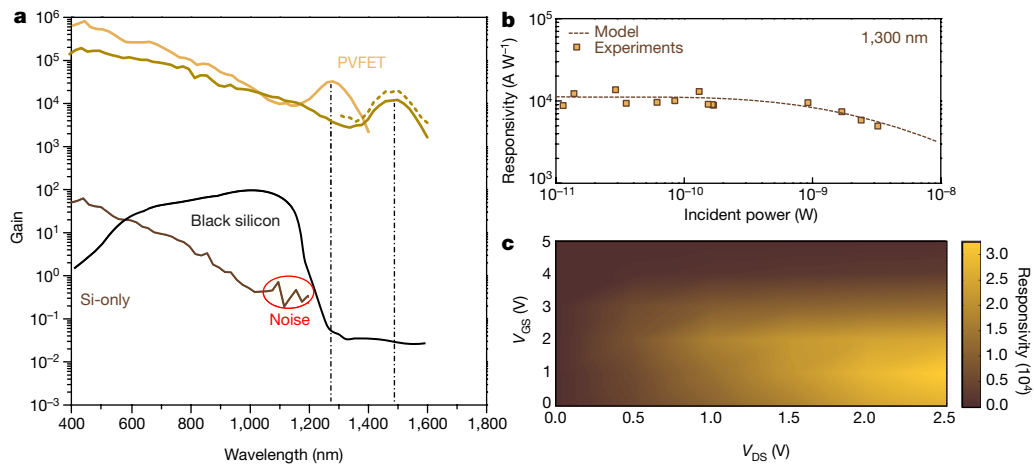
Figure 3 | Characterization of the PVFET. Spectral gain for the Si:CQD PVFET (for the photogate absorbing at 1,300 nm (light brown line) and 1,500 nm (gold line)), the silicon-only device and black silicon photodetectors. The PVFET was biased with $V_{GS} = 0$ V, and $V_{DS} = 2$ V (solid line) and $V_{DS} = 3$ V (dashed line). The vertical dash-dotted lines highlight the peaks in the PVFET curves. **b**, Responsivity (at 1,300-nm wavelength) as a function of the incident optical power P_{opt}. Experiments (squares) were fitted using an analytical model (dashed line) to compute the transconductive gain (gain $= h\nu/q \times V_{ph}g_m/P_{opt}$). **c**, Responsivity, under 1,300-nm illumination, as a function of bias. Responsivity follows the same trend as g_m (not plotted), saturating for V_{DS} higher than the saturation voltage (about 2 V) and vanishing at high V_{GS} (closed channel).

and we show (Fig. 2c), using the model of gain and bandwidth (see Supplementary Information section S9 for details of the model), that this value can in principle be further increased towards $10^5 \times 10^8 \, \text{s}^{-1}$.

The performance of the PVFET depends strongly on the quality of the Si:CQD rectifying junction (Supplementary Information sections S4, S11 and S12). The photovoltage that arises at the heterojunction interface is crucially determined—as in a solar cell, which also relies on the photovoltaic effect—by the rectification ratio of the junction; therefore, it is important to minimize the reverse saturation current of the junction (see Supplementary Information section S3). The PVFET converts the photovoltage signal to a photocurrent through the transconductance, which, in a junction transistor, also depends on the quality of the heterojunction. A highly rectifying, trap-free heterointerface must be engineered to produce efficient PVFETs. This approach distinguishes the device from previously reported photo-FETs based on CQDs. In these devices, gain comes from trap-assisted photoconduction; that is, the traps provided by the CQD film are responsible for

the long lifetime of the photocarriers recirculating in a high-mobility channel (for example, graphene or MoS$_2$). This produces a gain of $\tau_{l,CQD}/\tau_{t,channel}$ (the ratio between the lifetime of the CQD trap and the transit time of the charge in the channel). These devices do not require a rectifying photogate and their gain arises not from a transistor effect, but from a photoconductive one.

We fabricated Si:CQD PVFETs and characterized their performance. First, we investigated the spectral response of the detector. We report the gain (Fig. 3a; defined as the external quantum efficiency, which is given by the ratio between the numbers of photocarriers and incident photons) as a function of the wavelength. The device produces a gain of about 6×10^4 at the exciton. The excitonic peak (at either 1,300 nm or 1,500 nm) is characteristic of the CQD solid, and its energy is determined by the effect of quantum confinement, with greater spatial confinement increasing the effective bandgap of the CQD solid[22]. In Fig. 3a we compare the detector to a PVFET that lacks a CQD photogate (a silicon-only device), and to black silicon photodetectors[12].

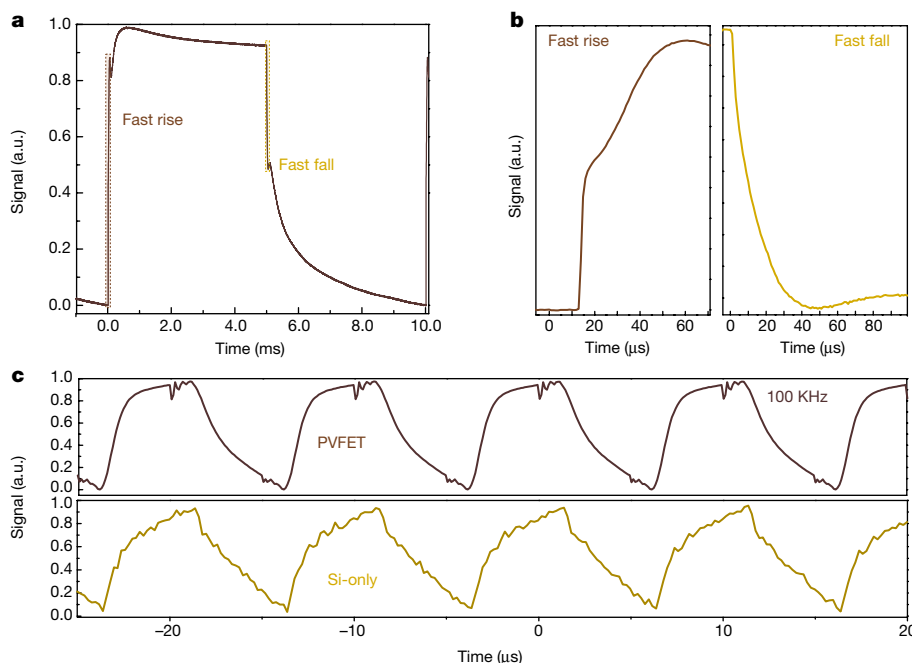**Figure 4 | Response time of the Si:CQD PVFET. a**, Rise and fall edges showing fast and slow components. **b**, Close ups of the fast components of the rise and fall edges (indicated by the shaded boxed regions in **a**; the time axis is arbitrary). **c**, Response to a 100-kHz modulated signal for the PVFET (top) and the silicon-only device (bottom). Time $= 0 \, \mu$s is chosen arbitrarily; a.u., arbitrary units.

The sensitivity of the silicon-only device vanishes beyond the bandgap of silicon at 1,100 nm. The gain of the PVFET remains high, owing to the high absorption of the CQD photogate at these longer wavelengths. The comparison with black silicon photodetectors reveals a responsivity at infrared wavelengths that is five orders of magnitude higher in the case of the PVFET.

We further characterized the PVFET, measuring its responsivity at 1,300 nm as a function of incident power. The gain of 10^4 at low intensity begins to roll off near about $2 \times 10^{-5}\,\mathrm{W\,cm^{-2}}$. Figure 3b shows this result, along with that predicted using the analytical model, in which the responsivity is calculated as $g_m V_{ph}/P_{opt}$. The device exhibits gain compression at high illumination, requiring offline nonlinearity correction, but also enabling increased dynamic range[21]. The responsivity of the PVFET as a function of V_{GS} and source–drain voltage V_{DS} (Fig. 3c) saturates for $V_{GS} > 2\,\mathrm{V}$, which corresponds to the saturation voltage of the transistor (for voltages higher than the saturation voltage, the transconductance g_m remains constant; see Supplementary Information section S2), and vanishes for increasing V_{GS}. Positive V_{GS} closes the channel (full depletion), which markedly decreases g_m (ref. 20): $g_m = G_o\big(1 - \sqrt{(V_{GS} - V_{bi})/V_{po}}\big)$, where G_o is a constant of the device, V_{bi} is the built-in voltage of the junction and V_{po} is the pinch-off voltage of the PVFET (more details on the static behaviour of the PVFET are provided in Supplementary Information section S2).

We proceeded to investigate the temporal response of the detector. Figure 4a, b shows the response of the PVFET to a square wave. It shows fast ($10\,\mu s$) fall and rise edges of the signal. This component of temporal response is compatible with sensing and imaging, addressing a wide range of consumer applications. The PVFET has a much faster response time than do traditional CQD-based photoconductors (about $100\,\mathrm{ms}$). A slower tail, attributable to defect states in the highly doped silicon substrates and the CQD bulk and interface, is also seen in the experimentally fabricated PVFETs. Removing these electronic states could increase the response time of PVFETs towards 1 GHz (the limit arising from g_m/C_{TOT}, as shown in Fig. 2), making them competitive with photodiodes and enabling applications such as time-of-flight sensing and machine vision[1]. In Fig. 4c, the signals acquired from the Si:CQD PVFET and the silicon-only device are compared. The two waveforms representing the response to a 100-kHz excitation are similar, with the PVFET presenting slightly sharper edges. (additional data are provided in Supplementary Information section S6). Notably, the addition of the CQD layer does not affect the transient response of the silicon device: it preserves its original speed, consistent with the fact that the PVFET gain mechanism does not rely on a memory effect from traps.

We measured the noise performance of the detector as a function of frequency, and found flicker noise at low frequencies (corner frequency at approximately 100 kHz) and a plateau at high frequencies that approaches the shot-noise limit (Supplementary Information section S5). The CQD photogate does not introduce additional noise to the silicon structure. We measured the noise current and obtained a detectivity of $D^* = 1.8 \times 10^{12}$ jones (1 jones = 1 cm $Hz^{1/2}\,W^{-1}$).

We also compared the device to previous CQD detectors. If we define a figure of merit $F = G_P \times BW/J_D^{1/2} = D^* \times BW$ that accounts for the responsivity (where BW is the bandwidth), the speed of response and the dark current density J_D, then the Si:CQD PVFET outperforms previous CQD-based detectors by at least one order of magnitude (Supplementary Information section S7). Traditional CQD-based photo-FETs and photoconductors are outperformed, owing to their lack of bandwidth; CQD diodes, which have a lower I_D, lack reponsivity and so have a lower F compared to the PVFET.

The Si:CQD PVFET has high gain ($>10^4$), even in the infrared (wavelengths of $>1,500$ nm), high speed (100 kHz) and contained dark current ($10^{-1}-10^1\,\mathrm{A\,cm^{-2}}$). This performance can be improved further by using advanced silicon processing. The advances reported here were possible only by devising an architecture that combines the benefits of silicon electronics with the emerging potential of CQDs. This architecture leverages a detection mechanism based on the photovoltaic effect combined with transconductive gain.

Online Content Methods, along with any additional Extended Data display items and Source Data, are available in the online version of the paper; references unique to these sections appear only in the online paper.

1. Soref, R. A. Silicon-based optoelectronics. *Proc. IEEE* **81,** 1687–1706 (1993).
2. Pavesi, L. & Lockwood, D. J. *Silicon Photonics* 239–268 (Springer, 2004).
3. Ma, L. L. *et al.* Wide-band 'black silicon' based on porous silicon. *Appl. Phys. Lett.* **88,** 171907 (2006).
4. Wang, J. & Lee, S. Ge-photodetectors for Si-based optoelectronic integration. *Sensors* **11,** 696–718 (2011).
5. Tanabe, K., Watanabe, K. & Arakawa, Y. III-V/Si hybrid photonic devices by direct fusion bonding. *Sci. Rep.* **2,** 349 (2012).
6. Soref, R. The impact of silicon photonics. *IEICE Trans. Electron.* **E91.C,** 129–130 (2008).
7. Masini, G., Colace, L. & Assanto, G. Si based optoelectronics for communications. *Mater. Sci. Eng. B* **89,** 2–9 (2002).
8. Masini, G., Colace, L. & Assanto, G. 2.5 Gbit/s polycrystalline germanium-on-silicon photodetector operating from 1.3 to 1.55 μm. *Appl. Phys. Lett.* **82,** 2524–2526 (2003).
9. Yablonovitch, E., Allara, D. L., Chang, C. C., Gmitter, T. & Bright, T. B. Unusually low surface-recombination velocity on silicon and germanium surfaces. *Phys. Rev. Lett.* **57,** 249–252 (1986).
10. Branz, H. M. *et al.* Nanostructured black silicon and the optical reflectance of graded-density surfaces. *Appl. Phys. Lett.* **94,** 231121 (2009).
11. Oh, J., Yuan, H.-C. & Branz, H. M. An 18.2%-efficient black-silicon solar cell achieved through control of carrier recombination in nanostructures. *Nat. Nanotechnol.* **7,** 743–748 (2012).
12. Carey, J. E., Crouch, C. H., Shen, M. & Mazur, E. Visible and near-infrared responsivity of femtosecond-laser microstructured silicon photodiodes. *Opt. Lett.* **30,** 1773–1775 (2005).
13. Konstantatos, G. & Sargent, E. H. Colloidal quantum dot photodetectors. *Infrared Phys. Technol.* **54,** 278–282 (2011).
14. Kamat, P. V. Quantum dot solar cells. Semiconductor nanocrystals as light harvesters. *J. Phys. Chem. C* **112,** 18737–18753 (2008).
15. Baskoutas, S. & Terzis, A. F. Size-dependent band gap of colloidal quantum dots. *J. Appl. Phys.* **99,** 013708 (2006).
16. Masala, S. *et al.* The silicon:colloidal quantum dot heterojunction. *Adv. Mater.* **27,** 7445–7450 (2015).
17. Adinolfi, V. *et al.* Photojunction field-effect transistor based on a colloidal quantum dot absorber channel layer. *ACS Nano* **9,** 356–362 (2015).
18. Konstantatos, G. *et al.* Hybrid graphene–quantum dot phototransistors with ultrahigh gain. *Nat. Nanotechnol.* **7,** 363–368 (2012).
19. Kufer, D. *et al.* Hybrid 2D–0D MoS₂–PbS quantum dot photodetectors. *Adv. Mater.* **27,** 176–180 (2015).
20. Sze, S. M. & Ng, K. K. *Physics of Semiconductor Devices* 3rd edn, Ch. 7 (Wiley, 2007).
21. Konstantatos, G. *et al.* Ultrasensitive solution-cast quantum dot photodetectors. *Nature* **442,** 180–183 (2006).
22. Lee, M. M., Teuscher, J., Miyasaka, T., Murakami, T. N. & Snaith, H. J. Efficient hybrid solar cells based on meso-superstructured organometal halide perovskites. *Science* **338,** 643–647 (2012).

Supplementary Information is available in the online version of the paper.

Author Contributions V.A. conceived the idea, designed the device, developed the process and fabricated the devices, and designed and performed all the experiments and the simulations and characterized the device in full. E.H.S. directed the research and contributed to the design of the experiments. V.A. and E.H.S. wrote the manuscript.

Author Information Reprints and permissions information is available at www.nature.com/reprints. The authors declare no competing financial interests. Readers are welcome to comment on the online version of the paper. Correspondence and requests for materials should be addressed to E.H.S. (ted.sargent@utoronto.com).

METHODS

PVFET fabrication. A silicon JFET (junction-FET) was fabricated using a standard VLSI (very large scale of integration) process. A 1.6-μm-thick epitaxial silicon layer (boron concentration, $\sim 5 \times 10^{15}$ cm^{-3}) was grown on top of a silicon substrate (300 μm; phosphorous concentration, $>10^{19}$ cm^{-3}). The source and drain were defined on the epitaxial channel using ion implantation and lithographic patterning of aluminium contacts (channel length, 5 μm; channel width, 1 mm). The source and drain were covered with a thick (>100 nm) layer of silicon nitride. The silicon surface was then cleaned using acetone and isopropanol, and the native surface oxide was removed by using buffered oxide etchant (BOE) diluted in water (1:10). Immediately afterwards, the surface was exposed to CH$_3$I using ultraviolet radiation to promote the reaction in an inert nitrogen atmosphere. Finally, a thin layer of CQD (~ 80 nm) was deposited by spin-coating inside a glove box. The CQDs were treated in the solid state using TBAI (tetrabutylammonium iodide) following an established procedure[23].

CQD synthesis. TMS (bis(trimethylsilyl)sulfide) (0.18 g, 1 mol) was added to ODE (1-octadecene) (10 ml), which was dried and degassed at 80 °C. A mixture of oleic acid (1.34 g, 4.8 mmol), PbO (0.45 g, 2.0 mmol) and ODE (14.2 g, 56.2 mmol) was heated to 95 °C under vacuum under Ar. The flask was heated to a temperature of 125 °C and the TMS/ODE mixture was injected. The temperature was then lowered to approximately 95 °C and the flask was cooled to 36 °C. The nanocrystals were precipitated with acetone (50 ml) and centrifuged. The precipitate was redispersed in toluene. The nanocrystals were precipitated again with acetone (20 ml), centrifuged (5 min) and then dispersed in toluene (~ 350 mg ml^{-1}). The quantum dots were then precipitated with methanol and dried under vacuum. They were then redispersed in toluene (100 mg ml^{-1}). The solutions used in the final materials processing were obtained by precipitating (using methanol) from this solution and redispersing in octane (50 mg ml^{-1}).

TCAD simulations. Numerical simulations were carried out using Synopsys Sentaurus TCAD (see Supplementary Information section S8). This software was used for the design of the silicon process (Sentaurus process) and for the simulation and the analysis of the PVFET (Sentaurus device).

Responsivity. The responsivity was measured using a SRS 830 lock-in amplifier. A time-modulated spectrally selected light signal was provided by using the combination of a monochromator and a mechanical chopper (frequency, 20 Hz). The incident power was measured using a Newport 1830 power meter. The incident light was controlled using an aperture. The incident power was defined by integrating the optical power density on the detector active area. The PVFET was biased using two Keithley 2400 Sourcemeters. The signal at the lock-in input was amplified using a SRS 570 current amplifier. The device was kept in a dark, shielded environment at atmospheric conditions.

Noise current measurements. The noise current was measured using a SRS 830 lock-in amplifier. The device was biased using a Keithley 2400 Sourcemeter. The device was kept in a shielded, dark enclosure.

Time response. The time response was acquired using an Agilent Infiniium digital oscilloscope. Photoexcitation was provided using a LED (wavelength, 450 nm; incident power, ~ 1 μW). The device was biased ($V_{DS} = 2.5$ V, $V_{GS} = 0$ V) using two Keithley 2400 SourceMeters.

Data availability. The data acquired for this study (data for Figs 3 and 4, noise measurements and responsivity as a function of frequency) are available at http://dx.doi.org/10.5061/dryad.s0k3h. Source Data for Figs 2–4 are available in the online version of the paper.

23. Tang, J. et al. Quantum junction solar cells. *Nano Lett.* **12,** 4889–4894 (2012).